Springer

KSME

Journal of Mechanical Science and Technology 32 (6) (2018) 2619~2627
www.springerlink.com/content/1738-494x(Print)/1976-3824(Online)
DOI 10.1007/s12206-018-0519-8

Shape optimization of flow channels based on lattice Boltzmann method †

Jungmin Park[1], Arman Safdari[2] and Kyung Chun Kim[2,*]

[1]*SFR NSSS System Design Division, Korea Atomic Energy Research Institute, Daejeon 34057, Korea*
[2]*School of Mechanical Engineering, Pusan National University, Busan 609-735, Korea*

(Manuscript Received July 7, 2017; Revised January 6, 2018; Accepted March 7, 2018)

Abstract

A new optimality criterion algorithm is presented for producing modified shape designs for fluid flow inside channels. To compute the fluid motion in a channel, the lattice Boltzmann method (LBM) was used based on D2Q9 and D3Q15 lattice spaces associated with the Bhatnagar-Gross-Krook (BGK) collision term. An experiential optimality method to design channels with the lowest pressure drop along the passage is introduced. The positions of solid cells and fluid cells are exchanged based on the strain rate tensor at the solid-fluid interface. To obtain the optimized shape, the cells are changed until the optimality condition is obtained with the restriction of constant fluid volume. Examples are presented to validate the algorithm, including an elbow tube as well as symmetrical and nonsymmetrical T-junction channels. The validation exercises demonstrate that the algorithm is suitable for optimal channel design.

Keywords: BGK; Channel; Lattice Boltzmann method; Optimal shape; Strain rate tensor

1. Introduction

One of the most popular methods for optimizing a fluid flow through a duct or industrial applications is the conventional trial-and error replacement approach, which has applications such as heat exchangers with channels, train heads, axial flow fan blades, and noise control. Some studies focus on shape optimization of the fluid flow [1-5], and there a great deal of effort is also devoted to developing numerical methods to solve flow optimization problems.

Borrvall et al. did the first study on shape optimization [6]. They proposed an optimal design method for Stokes flow problems by distributing inhomogeneous porous materials with a spatially varying Darcy permeability tensor and an artificial inverse permeability, which is proportional to the elemental thickness of a two-dimensional channel. Evgafov developed Borrvall's approach, which considered only porous materials, so that pure solid and fluid can appear in the optimization domain at the final stage of the optimization progress. However, the method could not be used for a widespread range of flows, and it works for very slow fluid flow [7, 8].

Gersborg-Hansen et al. investigated laminar incompressible fluid flow at low Reynolds number [9]. Moos et al. applied a new numerical approach to the topology optimization process instead of traditional methods such as evolution strategies or gradient-based methods [10]. Wang et al. introduced a heuristic optimality criterion algorithm for shape optimization based on the lattice Boltzmann method (LBM) [11]. They replaced the cells of fluid with solid units based on the value of dynamic pressure, which can be obtained from the density and velocity of fluid. Their method exchanges solid cells based on the maximum value of the shear stress among the solid nodes along the fluid-solid interface. It is practical to use LBM for complex fluid domains and simulating fluids at a kinetic level through the discrete Boltzmann equation. LBM is a well-known method with proven capability [11-13]. Two important characteristics are the kinetic nature and local dynamics of LBM, which make it more flexible in dealing with complex boundaries and parallelization of the algorithm.

In the present study, LBM was used to simulate the fluid flow through a complex geometry for two and three dimensions. A new algorithm is proposed for obtaining the optimized shape faster, transforming fluid cells into solid cells, and replacing inverse solid-fluid nodes based on just one criterion. In a previous study [11], two factors had to meet the optimization condition in order to convert the solid and fluid nodes. The first one is finding the node with the minimum dynamic pressure to change the fluid nodes to solid nodes, and the other one is obtaining the node with the maximum shear stress along the interface nodes in order to a change solid node to a fluid cell. However, in the present method, just one physical quantity is sufficient to replace the fluid and solid nodes. Therefore, an additional computational step at the macroscopic level is not required, and the computation time can be decreased. The new algorithm is also more straightforward.

*Corresponding author. Tel.: +82 51 510 2324, Fax.: +82 51 512 9835
E-mail address: kckim@pusan.ac.kr
† Recommended by Associate Editor Seongwon Kang

2. Mathematical model

2.1 Lattice Boltzmann method

Bhatnagar-Gross-Krook (BGK) LBM is based on a fluid distribution function that is applied for the momentum equation. Macroscopic fluid profiles such as pressure and velocity are found by solving the momentum equation. BGK is sometimes called the single relaxation time (SRT) method because it requires only one relaxation time for each vector of the lattice velocity. There are different patterns of LBM in the two-dimensional lattice units, such as D2Q5, D2Q7 and D2Q9. In LBM, the physical space is discretized into Cartesian grids. Each node in the LBM domain is related to its neighbors over lattice velocities. The D2Q9 model was implemented for its high accuracy among them. The governing equation of the LBM model is given by:

$$\frac{\partial f_i(\mathbf{x},t)}{\partial t} + \mathbf{c}\cdot\nabla f_i(\mathbf{x},t) = \Omega_i(\mathbf{x},t) + F_i(\mathbf{x},t) \tag{1}$$

where f_i is the density distribution function for particle velocity **c** in the space direction **x** at time t in a microscopic quantity, while i denotes the microscopic velocities of the unit lattice velocity. F_i is the external force in direction i and is assumed to be zero.

The collision term of the LBM equation (right-hand side of Eq. (1)) describes the collision of the particle distribution function, and a propagation term of the LBM (left-hand side of Eq. (1)) represents the movement of the density distribution function to the nearest neighbor lattice nodes after the collision term. The BGK model has a single relaxation time, and its discretized equilibrium distribution function for the D2Q9 equation is [14]:

$$\Omega_i = -\frac{f_i(\mathbf{x},t) - f_i^{eq}(\mathbf{x},t)}{\tau} \tag{2}$$

$$f_i^{eq}(\mathbf{x},t) = \rho\omega_i\left[1 + \frac{\mathbf{e_i}\cdot\mathbf{u}}{c_s^2} + \frac{1}{2}\frac{(\mathbf{e_i}\cdot\mathbf{u})^2}{c_s^2} - \frac{1}{2}\frac{u^2}{c_s^2}\right] \qquad c_s = \frac{\sqrt{3}}{3}. \tag{3}$$

In Eq. (2), f_i^{eq} is the equilibrium distribution function for the density associated with time t and position **x** and f is a scalar parameter representing species density at each local node. A macroscopic variable of a fluid such as the velocity, density or pressure can be derived from the distribution functions as following:

$$\rho = \sum_i f_i \tag{4}$$

$$\rho\mathbf{u} = \sum_i \mathbf{e_i} f_i \tag{5}$$

$$\mathrm{P} = \mathrm{c}_s^2\rho\,. \tag{6}$$

The relaxation time is a local number that is a function of space and time over the pressure and viscosity. Using Chapman-Enskog expansion, we can find the diffusion coefficient D in lattice units from the incompressible Navier-Stokes equations associated with the single dimensionless relaxation time τ for each component [15]:

$$\tau = 3\nu + \frac{1}{2}. \tag{7}$$

Let the lattice velocity be $\mathbf{c} = \Delta x / \Delta t$ which is assumed to be one because $\Delta x = \Delta t$. Therefore, for an incompressible Newtonian fluid, the weight coefficient ω_i must satisfy the following conditions:

$$\sum_i \omega_i = 1 \tag{8}$$

$$\sum_i \omega_i \vec{e}_i = 0\,. \tag{9}$$

In the propagation step of the LBM after the collision term, the analytical solution of the streaming term is:

$$f_i(\mathbf{x} + \mathbf{c}_i\delta t, t + \delta t) = f_i^{+}(\mathbf{x},t) \tag{10}$$

where $f_i^{+}(\mathbf{x},t)$ is the post-collision distribution function at **x** and t. In D2Q9, there are nine microscopic velocities that are commonly used for solving the fluid flow. The speed vector and the weight factors for both lattice arrangements are:

$$\mathbf{e_i} = \begin{bmatrix} 0 & 1 & 0 & -1 & 0 & 1 & -1 & -1 & 1 \\ 0 & 0 & 1 & 0 & -1 & 1 & 1 & -1 & -1 \end{bmatrix} \tag{11}$$

$$\omega_i = \left[\frac{4}{9} \quad \frac{1}{9} \quad \frac{1}{9} \quad \frac{1}{9} \quad \frac{1}{9} \quad \frac{1}{36} \quad \frac{1}{36} \quad \frac{1}{36} \quad \frac{1}{36}\right]. \tag{12}$$

The D3Q15 scheme of LBM is used because it is accurate enough to simulate the geometry. Furthermore, it has enough degrees of freedom to recover Navier-Stokes equation, although other schemes like D3Q19 and D3Q27 have higher accuracy compared with D3Q15. There are several reasons for applying D3Q15, such as less computation time and memory capacity in comparison with other schemes. The governing equation is similar to the D2Q9 velocity vector arrangement. The speed vectors and the weighting factors are:

$$\mathbf{e_i} = \begin{bmatrix} 0 & 1 & -1 & 0 & 0 & 0 & 0 & 1 & -1 & 1 & -1 & 1 & -1 & -1 & 1 \\ 0 & 0 & 0 & 1 & -1 & 0 & 0 & 1 & -1 & 1 & -1 & -1 & 1 & 1 & -1 \\ 0 & 0 & 0 & 0 & 0 & 1 & -1 & 1 & -1 & -1 & 1 & 1 & -1 & 1 & -1 \end{bmatrix} \tag{13}$$

$$\omega = \left[\frac{2}{9} \quad \frac{1}{9} \quad \frac{1}{9} \quad \frac{1}{9} \quad \frac{1}{9} \quad \frac{1}{9} \quad \frac{1}{9} \quad \frac{1}{72} \quad \frac{1}{72} \quad \frac{1}{72} \quad \frac{1}{72} \quad \frac{1}{72} \quad \frac{1}{72} \quad \frac{1}{72} \quad \frac{1}{72}\right]. \tag{14}$$

2.2 Strain rate tensor

The main difference between the method by Wang et al. [11] and this study is the optimality criterion. Wang et al. [11]

Table 1. Simulation setup.

Channel	Grids	Re	Viscosity [lu^2/ts]	Velocity [lu/ts]
Elbow	100 x 100	20	0.04	0.04
T-junction	200 x 200	20	0.04	0.02
Non-sym. T-junction	200 x 200	20	0.04	0.02
Square duct	200 x 200 x 200	100	0.04	0.1

employed two criteria: The shear stress and the dynamic pressure at the solid and fluid interfaces. In contrast, the strain rate tensor is the only one criterion in the present study. This physical measure defines the amount of change of the deformation of a substance in the neighborhood of a certain node.

The strain rate tensor is a kinematic property that defines the macroscopic change of the material. There is no dependency between the strain rate tensor and the nature of the material or between the forces and stresses that may be acting on it. In the LBM, the strain rate tensor can be obtained from the density distribution function for the macro quantities by mathematical analysis using Chapman-Enskog and Taylor expansion as follows [16]:

$$S_{i,j} = \varepsilon \sum_{\alpha} \mathbf{e}_{\alpha,\mathbf{i}} \mathbf{e}_{\alpha,\mathbf{j}} \left(f_i - f_i^{eq} \right), \tag{15}$$

$$\varepsilon = \frac{-2}{2\rho c^2 \tau \delta t}. \tag{16}$$

Eq. (15) shows the importance of the distinction between equilibrium and density distribution functions. The key step in optimizing the shape of a channel is determining the strain tensor and finding the nodes having maximum and minimum values of the strain tensor along the fluid-solid interfaces.

2.3 Simulation setup

In this study, three geometries for 2D and one for 3D geometry are simulated. The initial shapes are presented in Fig. 1. The inlet area of 3D square duct has same height of 2D Elbow channel. The detail simulation parameters are presented in Table 1. The kinematic viscosity in Table 1 has units lu^2/ts. Lu is the lattice unit which is the length between two grids, and ts represents discretized time step. For pressure P, Zou-He conditions are applied with density $\rho = 1$.

Zou-He boundary conditions are employed for the pressure and velocity boundary conditions. It is known that Zou-He boundary conditions have second-order errors for 2D and 3D square duct flow [17]. Full-way bounce-back scheme is applied along the wall for no-slip condition. Bounce-back scheme is easy to implement and robust for the complex geometry which can be observed during the optimization process.

2.4 Optimization process

Fig. 2 shows the simple concept of exchanging fluid-solid

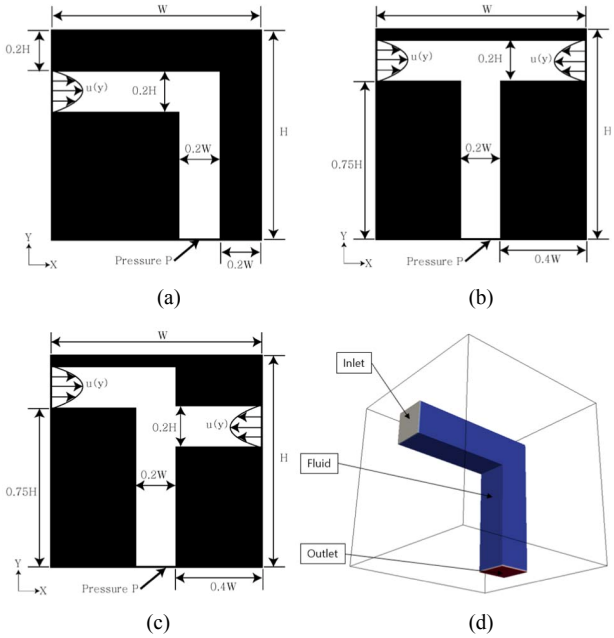

Fig. 1. Simulation geometries: (a) 2D elbow; (b) 2D symmetric T-junction; (c) 2D nonsymmetrical T-junction; (d) 3D square duct.

cells. The fluid node with lowest strain rate tensor is changed into solid node, and the solid node near the fluid node with highest strain rate tensor becomes the fluid node.

Fig. 3 shows a flowchart of the simulation procedure, and the detail simulation steps are as follows:

(1) Solid and fluid nodes need to be defined in the simulation domain, and the density and kinematic viscosity are the initial input data. The density and viscosity of the fluid are $\rho = 1$ and $v = 0.04$.

(2) At a certain time step, the time derivatives of fluid properties such as the velocity and pressure become very small after applying the propagation step, the collision term, and the boundary conditions at the inlet, outlet, and walls. Therefore, the fluid simulation is paused when a fixed flow is obtained. This happens when the average speeds of the flow in two time steps in all the computational cells are smaller than 1×10^{-8}:

$$u_{ave} = \frac{1}{N} \sum \left| \vec{u}^{n+1} - \vec{u}^{n} \right| \tag{17}$$

where N is the total number of computational cells in the domain.

(3) After finding the solid-fluid interfaces and applying Eq. (15), a number of cells with the lowest strain rate tensor are changed to solid, and the same number of solid cells with neighbor cells that have a higher strain rate tensor are changed to fluid, thus creating a new channel shape. To maintain the fluid and solid volumes in the simulation domain, the numbers of cells changing from fluid to solid and solid to fluid are equal. The accuracy of the algorithm is higher if a small amount of cells is replaced for each iteration. However, as the number of simulation steps increases, which increases the

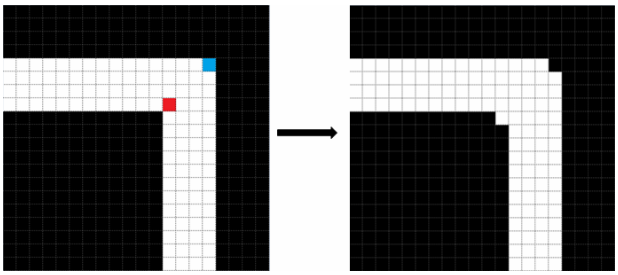

Fig. 2. Simple concept of the exchanging fluid-solid cell. Red square is the cell with the highest strain rate tensor, and blue one has the lowest strain rate tensor.

computation time, a certain number of solid-fluid cell pairs are replaced in each simulation time step. The values of exchanging cells should be small enough for the fluid flow to converge after generating a new shape. In this simulation, the proportion of exchanging cell pairs is between 2 % and 5 % of the total interface cells.

(4) In this stage, a new channel shape with a new set of solid and fluid cells needs to be initialized. Therefore, the fluid properties and boundary conditions are adjusted again. To reach steady-state conditions Eq. (17) faster for the new shape, the previous properties of the fluid are input as initial data, and the velocity of a fluid cell that was changed from solid to fluid is zero. To simulate the stable fluid flow, the initial value of the velocity profile should be zero after exchanging cells.

(5) After recalculation of the fluid flow, the stability tolerance of the proposed algorithm and pressure drop should be checked. If the tolerance of the heuristic procedure meets expectations, the results can be exported, and the optimized shape is plotted. If not, the calculation starts again from step 3. The procedure is stopped when a fixed pressure drop is obtained. This happens when the average pressure across the system approaches the maximum tolerance 1×10^{-5}:

$$\frac{1}{N}\sum\left|\Delta P^{t+n\delta t}-\Delta P^{t}\right|\le E_{tolerance} \tag{18}$$

where N is the total number of computational cells in the domain, and n is 10.

3. Results and discussion

One of most challenging topics related to fluid flow inside a channel or tube is finding a way to reduce the pressure or viscous dissipation. The controlled distribution of a fluid into a tube is an important issue for various aspects of performance. Many industrial and engineering applications need an optimized design that has less friction between the fluid and solid wall. We expected the pressure drop or flow resistance to decrease after applying the proposed algorithm. Three fluid flow shapes shown in Fig. 1 were tested to validate the algorithm.

3.1 Validation

To validate our algorithm before presenting results of channels we compared results between our algorithm and Wang et al. [11]. With the geometry shown in Fig. 4, the validation was performed. The numerical parameters are as following: Grid size is 200 x 200, inlet velocity is equal to 0.04 lu/ts, the viscosity ν is equal to 0.04 lu^2/ts, and its Reynolds number is 40. It is observed that our algorithm can obtain nearly same final shape with Wang et al.'s result as shown in Fig. 5. The pressure drop improvement from Wang et al. [11] was 67 % and our result improved 66 %. The small difference comes from the different criteria being used for both studies.

In order to investigate the effect of grid resolution for the optimization algorithm, the comparative tests are carried out.

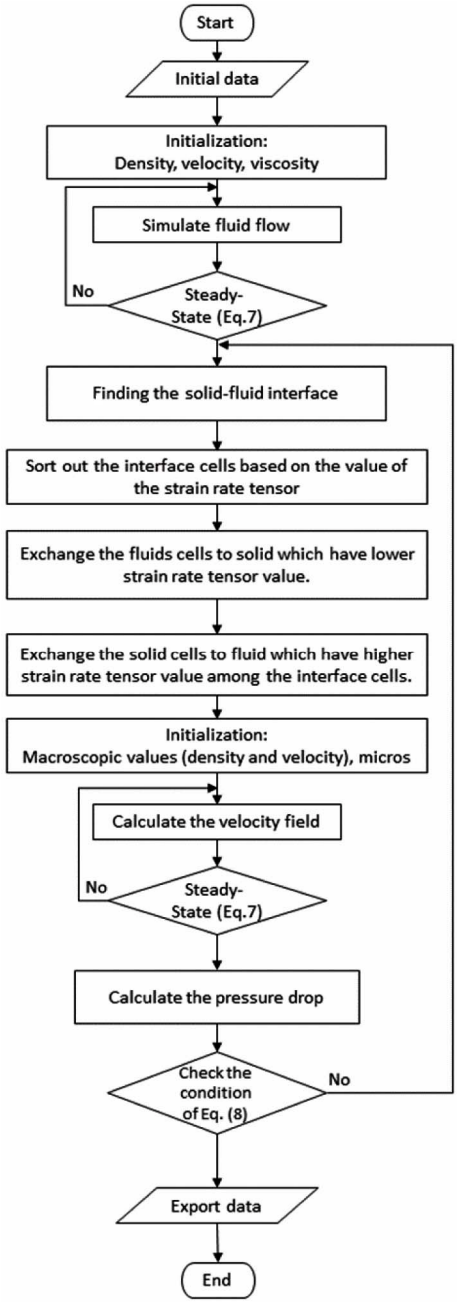

Fig. 3. Flow chart for the optimization process.

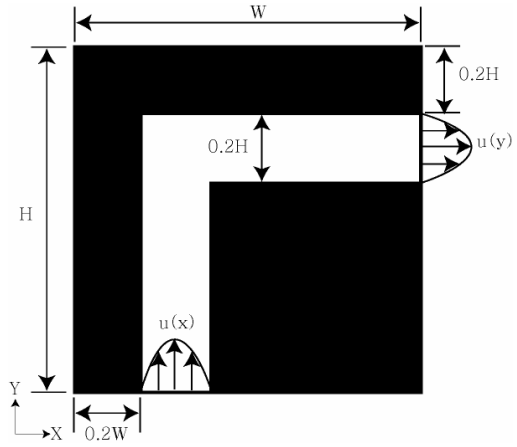

Fig. 4. Simulation setup. Re = 40, grid = 200 x 200, inlet u_0 = 0.04 lu/ts.

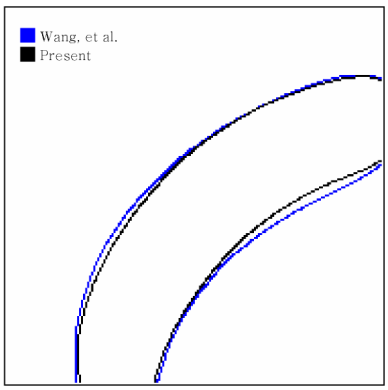

Fig. 5. Comparison with the result of Wang et al. [11].

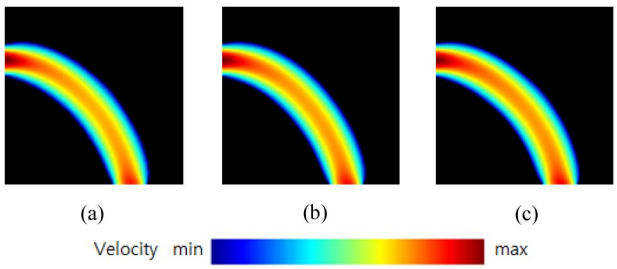

Fig. 6. Optimized elbow shapes at Re = 40 with different grid sizes: (a) 100 x 100; (b) 200 x 200; (c) 400 x 400.

Three cases of lattice sizes (100 x 100, 200 x 200, 400 x 400) for the elbow geometry (Fig. 1(a)) are compared. Each case keeps the numerical parameters identical other than the lattice size. Fig. 6 shows that almost identical results are represented. It is surely considered that the grid resolution has less effect in the optimized shapes earned from the heuristic algorithm.

To validate the code can predict correct flow behaviors such as Dean vortex in the curved duct, a 3D simulation has conducted. Fig. 7 shows the vorticity in Z axis (the direction of flow) inside the optimized 3D duct. The flow is simulated for Re = 100 with 200 x 200 x 200. The Dean number is equal to 55, which is in the range where the dean vortices are predicted,

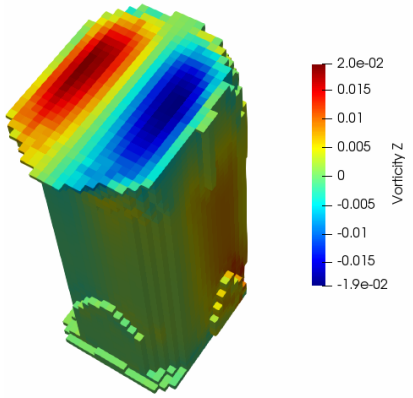

Fig. 7. Dean vortices in the curved duct at Dean number 55.

Fig. 8. Images of shape development between the first and 150th iterations: (a) 1st step; (b) 50th step; (c) 80th step; (d) 150th step.

so is the result.

3.2 Elbow channel

The bend or curve in the channel causes viscous dissipation and energy loss when fluid is flowing in an elbow tube. We applied our optimization procedure to reduce the pressure drop and improve the design to reach the most uniform velocity along the channel. Fig. 1(a) shows the simulation domain. The height and width of the whole domain are divided into 100 nodes. We selected an odd number of nodes for the inlet boundary conditions to imply a symmetrical parabolic velocity. Therefore, 21 nodes were chosen as the inlet boundary nodes, and the same length was used for the outlet boundary conditions. Using the viscosity v and inlet length L_i, the corresponding velocity U_0 can be obtained from the Reynolds number $Re = L_i U_0 / v$.

Fig. 8 illustrates the shape development and algorithm process. The inner and outer edges of the bend gradually become smoother, and the distance between the inlet and outlet flows becomes smaller and smaller until it reaches the steady-state shape, where the characteristics of the fluid such as the flow velocity do not change as time passes. Fig. 9 shows that the singularity in velocity field decreases over time and is well maintained when the optimized shape appears. Also, the flow turns slowly rather than abruptly.

Fig. 10 shows the pressure drop of the system with respect to time. The pressure drop is normalized. The pressure drop decreases up to 0.341 in the final stage. The results prove that the total pressure of the optimized shape is decreased by over 66 % compared to the fist shape of the tube, and it tends to be

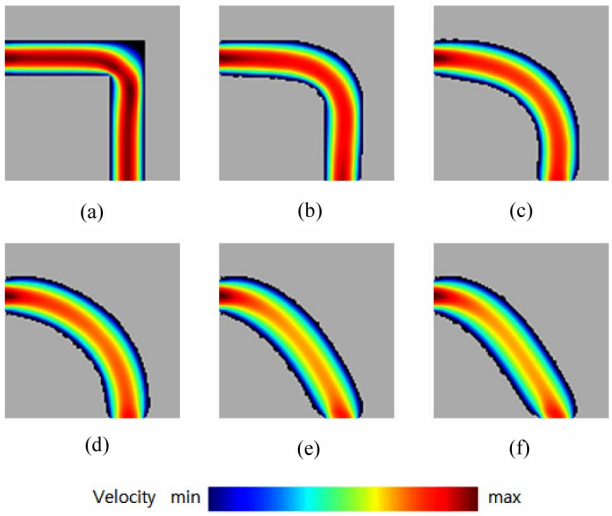

Fig. 9. The development of the flow field between the first and 140th iterations: (a) 1st step; (b) 11th step; (c) 37th step; (d) 60th step; (e) 100th step; (f) 140th step.

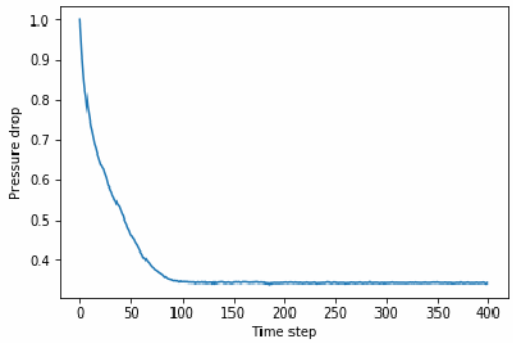

Fig. 10. Pressure drop with respect to time for Re = 20 through the elbow channel.

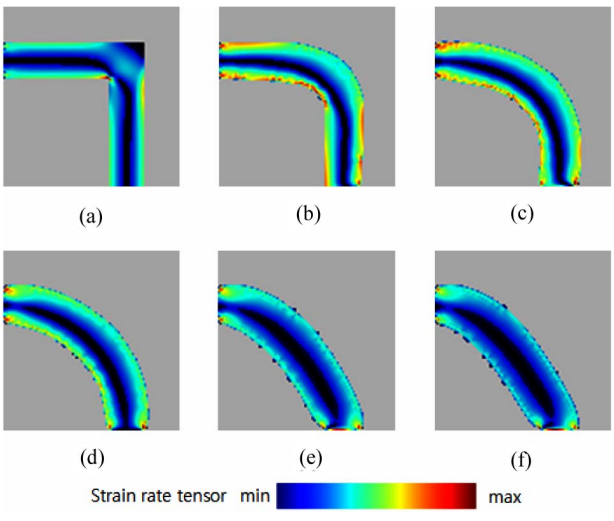

Fig. 11. Development of strain rate tensor between the first and 150th iterations: (a) 1st step; (b) 11th step; (c) 37th step; (d) 60th step; (e) 100th step; (f) 140th step.

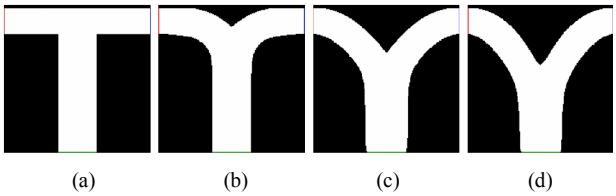

Fig. 12. Symmetrical T-junction shape development snapshots between the first and 380th iterations: (a) 1st step; (b) 40th step; (c) 190th step; (d) 380th step.

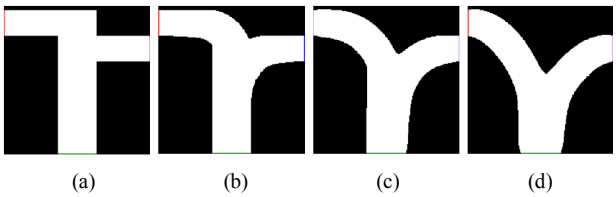

Fig. 13. Nonsymmetrical T-junction shape development snapshots between the first and 1920th iterations: (a) 1st step; (b) 100th step; (c) 400th step; (d) 1920th step.

stable after reaching a certain pressure drop.

Fig. 11 represents the strain rate values during the shape development. The strain rate is defined as the degree of deformation around the cells at the interface. Because of the fluid element friction, any change in the deformation increases the interior tensor forces, which increase to oppose the deformation. The viscous tensor is linear with respect to the strain rate tensor. High viscous stress occurs in the interface cells where the rate of the strain tensor is high. As a result, in the initial shape of the development, a high rate of the strain tensor occurs at the sharp point of the outer corner in the fluid domain. However, the rate of the strain tensor spreads gradually and turns slowly along the interface.

3.3 Symmetrical and nonsymmetrical T-junction channel

Fig. 1 shows the initial profile of symmetrical (Fig. 1(b)) and nonsymmetrical (Fig. 1(c)) T-junctions with merging channel flow, which are commonly used in industrial and research applications. A grid size of 200×200 was chosen for both cases. The inlet boundaries comprised 70 cells, and the length of the outlet was $0.25\times L_i+1$, where L_i is the total length of the simulation domain in the y direction. Both inlets on the right and left are equal and have the same absolute velocity profiles with opposite directions. Dirichlet boundary conditions with constant pressure are applied for the outlet. Therefore, the specified density ρ is set to one, and the velocity profile is computed from this boundary. U_0 is obtained in the same way from the Reynolds number. Fig. 12 shows the shape development of the symmetrical T-junction, and Fig. 13 shows the nonsymmetrical T-junction.

Fig. 14 illustrates the total pressure drop between the inlets and the outlet as a function of the iterations for the symmetrical and nonsymmetrical T-junctions. The total pressure drop of the initial shape for the symmetrical T-junction is 1.0 and it

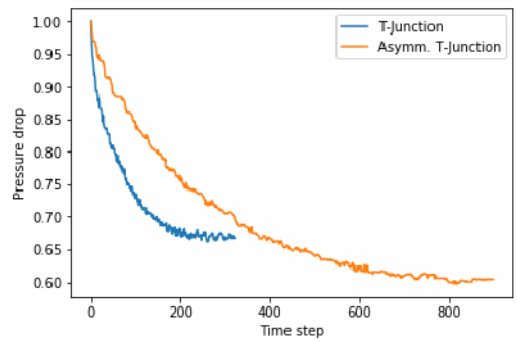

Fig. 14. Pressure drop with respect to time for Re = 20 through the symmetrical T-junction channel and the nonsymmetrical T-junction channel.

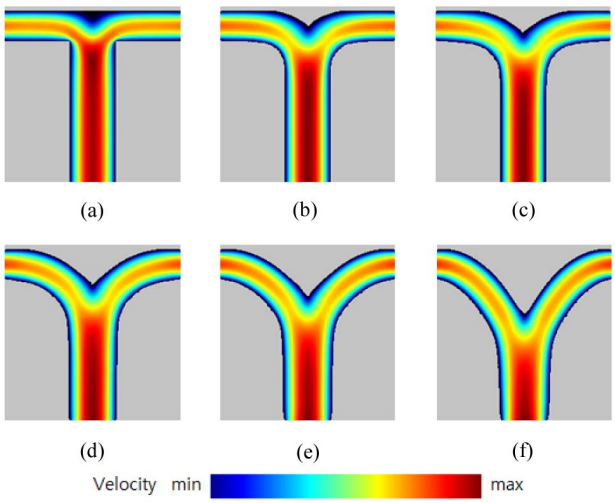

Fig. 15. Development of flow field in the symmetrical T-junction shape between the first and 300th iterations: (a) 1st step; (b) 20th step; (c) 40th step; (d) 100th step; (e) 160th step; (f) 300th step.

drops to 0.667 for the final shape. The improvement of total pressure drop is 34 % compare to the initial shape. The same behavior of pressure reduction occurs in the nonsymmetrical T-junction. The total pressure drop reduced up to 40 % for the nonsymmetrical T-junction channel.

Figs. 15 and 16 show the corresponding flow fields for symmetrical and nonsymmetrical T-junctions as a function of the development time. In the figures, it is easy to see that the two right-angle corners gradually disappear with increasing iterations and become circular. Fluid cells with a low strain rate tensor in the position of joining fluids are replaced by the solid nodes. Therefore, the void volume between the junctions is used effectively, and dead zones become solid. After the pressure drop across the system converges to a certain point, the symmetrical and nonsymmetrical T-junction shapes change to a Y-shaped junction.

Figs. 17 and 18 show the value of the strain rate tensor as a function of the development time for symmetrical and non-symmetrical T-junctions at *Re = 20*. Low values of the strain rate tensor occur in the void volume area, and a high strain

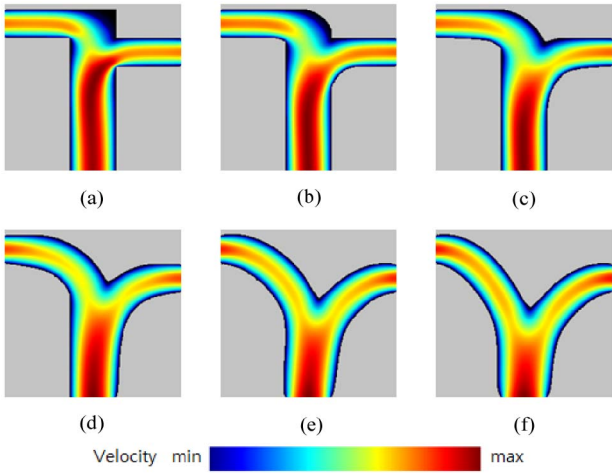

Fig. 16. Development of flow field in the nonsymmetrical T-junction shape between the first and 300th iterations: (a) 1st step; (b) 30th step; (c) 100th step; (d) 300th step; (e) 600th step; (f) 1000th step.

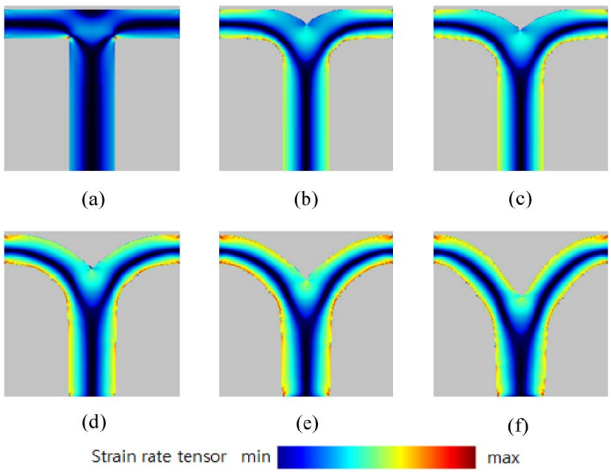

Fig. 17. Development of strain rate tensor in the symmetrical T-junction shape between the first and 300th iterations: (a) 1st step; (b) 20th step; (c) 40th step; (d) 100th step; (e) 160th step; (f) 300th step.

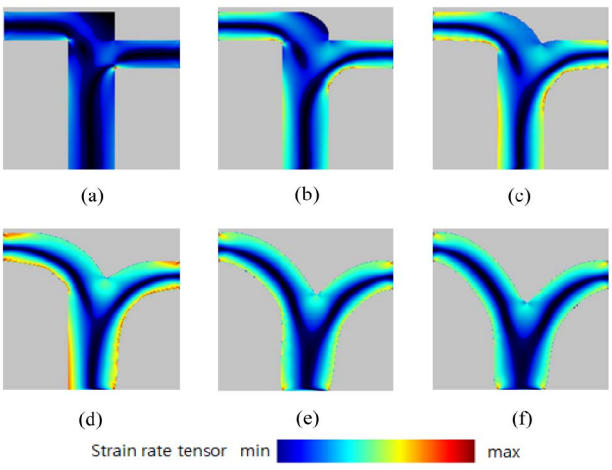

Fig. 18. The development of strain rate tensor in the nonsymmetrical T-junction shape between the first and 1000th iterations: (a) 1st step; (b) 30th step; (c) 100th step; (d) 300th step; (e) 600th step; (f) 1000th step.

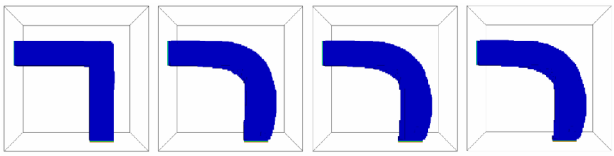

(a) (b) (c) (d)

Fig. 19. Shape change at different iterations: (a) 1st; (b) 60th; (c) 120th; (d) 160th.

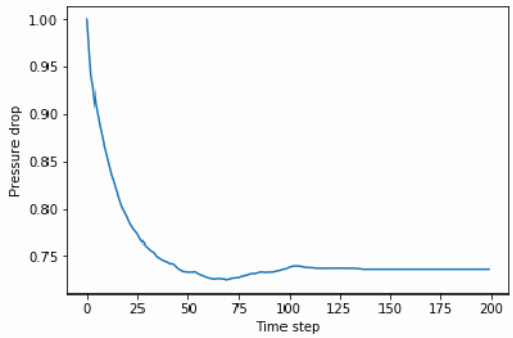

Fig. 20. Pressure drop with respect to time for Re = 100 in the 3D elbow duct.

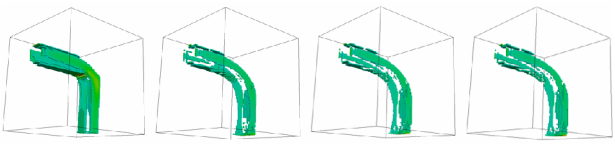

(a) (b) (c) (d)

Fig. 21. Development of strain rate tensor in elbow duct.

tensor occurs near the sharp edges. However, by applying the algorithm, the strain rate tensor turns gradually rather than abruptly in the last shape development for both T-junctions.

3.4 Three-dimensional elbow duct

The inlet velocity boundary condition is assumed to be a fully developed flow that has a parabolic shape, which is commonly observed in industrial and research applications. The Reynolds number is set as 100, from which the maximum velocity U_0 can be calculated. A rectangular elbow duct is modeled to test the method, and its cross-section is shown in Fig. 1(d). A grid size of 200×200×200 was chosen, of which 40 cells are selected for the inlet boundary condition, and an equal number of inlet nodes is chosen for the outlet boundary condition. Zero gradient pressure was set at the outlet of the duct.

Fig. 19 shows that the sharp edges of the duct become smoother during the optimization progress, and the outlines change to a round shape. Fig. 20 shows the pressure of the elbow duct decreased sharply to 0.736 at the 50th iteration, and it becomes smooth when it reaches steady state. There is a direct relation between the pressure and the development of the shape. Finally, the pressure fell about 27 % compared with the first shape of the elbow duct. In order to illustrate how the strain rate tensor distributes through the elbow duct, several images of strain rate tensor are shown in Fig. 21. The strain rate tensor becomes smaller with time step goes on.

4. Conclusions

We presented an empirical optimality algorithm for designing a fluid flow channel using LBM. The positions of exchanging solid cells are obtained based on the strain rate tensor along the interface. Fluid cells with a low strain tensor are exchanged with solid cells, and the solid cells near cells with a high strain tensor are exchanged with fluid cells. The pressure drops gradually while the channel shape evolves to the final structure. We presented three different channel shapes and implemented the algorithm accordingly. The results prove the capability of the algorithm in fluid problems. The strain rate tensor along the interface is the only optimality factor needed to replace the cells. Therefore, this heuristic optimality criterion needs fewer equations to find the cells to be exchanged and is also easy to perform.

Acknowledgments

This study was supported by the National Research Foundation of Korea (NRF) grant funded by the Korean government (MSIT) through GCRC-SOP (No. 2011-0030013).

Nomenclature

f_i	: ith density distribution function
$\mathbf{x}$	: Particle position
$\mathbf{c}$	: Particle velocity
Δx	: Unit grid length in lattice unit
Δt	: Unit time step in lattice unit
t	: Time
Ω_i	: Collision term
f_i^{eq}	: Equilibrium density distribution function
τ	: Relaxation time
$\mathbf{e}_i$	: Unit velocity vector
f_i^+	: Post-collision distribution function
$S_{i,j}$	: Strain rate tensor
v	: Viscosity
N	: Total number of cells in the domain
P	: Pressure of the flow
ΔP	: Pressure difference from the initial state
N	: Total number of cells in the domain
ω	: Weight coefficient
$\mathbf{F}_i$	: External force

References

[1] D. Tondeur, Y. Fan and L. Luo, Flow distribution and pressure drop in 2D meshed channel circuits, *Chemical Engineering Science*, 66 (2011) 15-26.

[2] C. Wagner, G. M. Horstmann, S. Herzog, D. Jakubek and S. Rutschmann, Shape optimization of train heads with respect to the aerodynamic loads of track side objects, *International Journal of Railway Technology*, 3 (2014) 83-104.
[3] P. Song and J. Sun, Blade shape optimization for transonic axial flow fan, *Journal of Mechanical Science and Technology*, 29 (2015) 931-938.
[4] E. Vergnault and P. Sagaut, An adjoint-based lattice Boltzmann method for noise control problems, *Journal of Computational Physics*, 276 (2014) 39-61.
[5] S. Kreissl, G. Pingen and K. Maute, An explicit level set approach for generalized shape optimization of fluids with the lattice Boltzmann method, *International Journal for Numerical Methods in Fluids*, 65 (2011) 496-519.
[6] T. Borrvall and J. Petersson, Topology optimization of fluids in Stokes flow, *International Journal for Numerical Methods in Fluids*, 41 (2003) 77-107.
[7] A. Evgrafov, The limits of porous materials in the topology optimization of Stokes flows, *Applied Mathematics and Optimization*, 52 (2005) 263-277.
[8] A. Evgrafov, Topology optimization of slightly compressible fluids, *Journal of Applied Mathematics and Mechanics*, 86 (2006) 46-62.
[9] A. Gersborg-Hansen, O. Sigmund and R. B. Haber, Topology optimization of channel flow problems, *Structural and Multidisciplinary Optimization*, 30 (2005) 181-192.
[10] O. Moos, F. R. Klimetzek and R. Rossmann, Bionic optimization of air-guiding systems, *SAE Technical Paper* (2004).
[11] L. Wang, Y. Fan and L. Luo, Heuristic optimality criterion algorithm for shape design of fluid flow, *Journal of Computational Physics*, 229 (2010) 8031-8044.
[12] L. Luo, M. Wei, Y. Fan and G. Flamant, Heuristic shape optimization of baffled fluid distributor for uniform flow distribution, *Chemical Engineering Science*, 123 (2015) 542-556.
[13] A. Safdari and K. C. Kim, Lattice Boltzmann simulation of the three-dimensional motions of particles with various density ratios in lid-driven cavity flow, *Applied Mathematics and Computation*, 265 (2015) 826-843.
[14] A. Safdari and K. C. Kim, Lattice Boltzmann simulation of solid particles behavior in a three-dimensional lid-driven cavity flow, *Computers & Mathematics with Applications*, 68 (2014) 606-621.
[15] G. McNamara and B. Alder, Analysis of the lattice Boltzmann treatment of hydrodynamics, *Physica A: Statistical Mechanics and its Applications*, 194 (1993) 218-228.
[16] J. Li and Z. Wang, An alternative scheme to calculate the strain rate tensor for the LES applications in the LBM, *Mathematical Problems in Engineering* (2010) 13.
[17] Q. Zou and X. He, On pressure and velocity boundary conditions for the lattice Boltzmann BGK model, *Physics of Fluids,* 9 (1997) 1591-1598.

Jungmin Park is a researcher in Korea Atomic Energy Research Institute. His main research interests are application of computational fluid dynamics in energy conversion system and organic Rankine cycle system. He is currently working on designing decay heat removal system.

Kyung Chun Kim is a Professor at the School of Mechanical Engineering of Pusan National University in Korea. He obtained his Ph.D. from the Korea Advanced Institute of Science and Technology (KAIST), Korea, in 1987. He was selected as a Member of the National Academy of Engineering of Korea in 2004. His research interests include flow measurements based on PIV/LIF, POCT development, wind turbines, and organic Rankine cycle system.